MDPI

Article

Enhanced Photoluminescence of Electrodeposited Europium Complex on Bare and Terpyridine-Functionalized Porous Si Surfaces

Min Hee Joo [1,2], So Jeong Park [1], Hye Ji Jang [1], Sung-Min Hong [1,2], Choong Kyun Rhee [1] and Youngku Sohn [1,2,*]

[1] Department of Chemistry, Chungnam National University, Daejeon 34134, Korea; wnalsgml4803@naver.com (M.H.J.); jsjs5921@naver.com (S.J.P.); gpwldndud@naver.com (H.J.J.); qwqe212@naver.com (S.-M.H.); ckrhee@cnu.ac.kr (C.K.R.)

[2] Department of Chemical Engineering and Applied Chemistry, Chungnam National University, Daejeon 34134, Korea

* Correspondence: youngkusohn@cnu.ac.kr; Tel.: +82-42-821-6548

Abstract: The trivalent Eu(III) ion exhibits unique red luminescence and plays an significant role in the display industry. Herein, the amperometry electrodeposition method was employed to electrodeposit Eu(III) materials on porous Si and terpyridine-functionalized Si surfaces. The electrodeposited materials were fully characterized by scanning electron microscopy, X-ray diffraction crystallography, Fourier-transform infrared spectroscopy, and X-ray photoelectron spectroscopy. Photoluminescence (PL) spectroscopy revealed that PL signals were substantially increased upon deposition on porous Si surfaces. PL signals were mainly due to direct excitation and charge-transfer-indirect excitations before and after thermal annealing, respectively. The as-electrodeposited materials were of a Eu(III) complex consisting of OH, H_2O, NO_3^-, and CO_3^{2-} groups. The complex was transformed to Eu_2O_3 upon thermal annealing at 700 °C. The electrodeposition on porous surfaces provide invaluable information on the fabrication of thin films for displays, as well as photoelectrodes for catalyst applications.

Keywords: porous Si; photoluminescence; europium; lanthanide; electrodeposition; terpyridine; functionalization

1. Introduction

Porous silicon (PS) is known to show unique physicochemical properties and a high surface area [1–5]. The pores have commonly been prepared by electrochemical anodization process in a hydrofluoric acid (HF) solution by varying many experimental parameters such as concentration, organic-solvent additive, time, and applied potential [6,7]. The properties have consequently been determined by the finally achieved pore sizes and depths. The application areas are very wide, and include sensors, catalysts, solar cells, and charge storages [8–17]. For sensors, Ramírez-González et al. controlled the thickness of the PS layer and tested ethanol-sensing performance by measuring conductivity. They showed that the thickness is an important factor for a target-sensing gas [14]. Dwivedi et al. prepared TiO_2 nanotube-decorated PS, and showed that the heterojunction exhibited a selective ethanol-sensing performance (with sub-ppm level down to 0.5 ppm) and a good linear response at low detection level [15]. For catalyst applications, Kim et al. used PS nanoparticles (NPs) for embedding Pd (~12 nm) and superparamagnetic γ-Fe_2O_3 (~7 nm) NPs [16]. They demonstrated that the nanocomposites showed an excellent catalytic performance for the reduction of 4-nitrophenol to 4-aminophenol by $NaBH_4$. For solar cells, Sundarapura et al. prepared an anodic SiO_2 layer on a PS surface, and demonstrated that the solar-cell efficiency was significantly improved [13]. For energy storage, Ortaboy et al. synthesized MnO_x-decorated carbonized porous Si nanowire, and showed that the PS nanowire-based pseudocapacitor electrode had a specific capacitance of 635 F g^{-1},

areal power of 100 mW cm^{-2}, and energy of 0.46 mW h cm^{-2} [17]. They also reported a power density of 25 kW kg^{-1} and an energy density of 261 W h kg^{-1} at 0.2 mA/cm^2, and a large potential window of 3.6 V. Surface functionalization on Si has also widely been demonstrated to widen the application areas and performances [18–20]. Yaghoubi et al. prepared a PS by the electrochemical etching method and modified with lectins via amino-silane functionalization followed by glutaaldehyde incubation [20]. They demonstrated that a lectin-conjugated PS showed good biosensing performances for label-free and real-time detection of *Escherichia coli* and *Staphylococcus aureus* by reflectometric interference Fourier transform spectroscopy.

In the present study, the electrodeposition method was employed to embed electrodeposited materials inside the pores of a PS and to examine new characteristics arising from the newly developed PS materials. In addition, surface functionalization was performed to further modify the surface property on electrodeposition. The Eu(III) ion was selected because it exhibits strong red luminescence and depends on local environment [21]. Therefore, luminescence profiles were examined, and consequently, dramatically enhanced luminescence characteristics was observed. The newly reported results provide valuable information on the development of thin-film display materials, as well as thin films for other application areas, such as catalyst electrodes.

2. Materials and Methods

Chemicals of Eu(III) nitrate hexahydrate (99.9%, Alfa Aesar, Karlsruhe, Germany), sodium perchlorate (NaClO$_4$, ≥98.0%, Sigma-Aldrich, St. Louis, MO, USA), (3-aminopropyl) trimethoxysilane (APTMS, 97%, Sigma-Aldrich), and 2,2′:6′,2″-terpyridine-4′-carboxylic acid (Tpy-COOH, 95%, Alfa Aesar) were used as received without further purification. An Si wafer (<100> B-doped p-type, Siltron Inc., Gumi, Korea) was cut to a size of 20 mm × 20 mm and precleaned with isopropyl alcohol and deionized water, repeatedly. The precleaned Si wafer was dipped in a solution of H$_2$O:H$_2$O$_2$:NH$_4$OH (5:1:1 *v/v*) for 15 min, then dipped again in a 2% HF solution for 30 min, and dried under an infrared lamp. Gold (Au) sputtering was performed on the Si wafer at a current of 5 mA for 90 s, and then thermal treated at 700 °C for 2 h in a furnace. For the fabrication of a porous Si (PS), the Au-deposited Si wafer was dipped in a 5% HF solution for 48 h, and then cleaned with deionized water. In the second etching step, the pre-etched Si wafer was used as an anode. A carbon rod was used as a cathode with an applied potential of 30.0 V for 1 h in an etching solution (ethanol:deionized water:HF = 2:1:1 molar ratio). Au nanoparticle residues on the Si wafer were further removed by dipping in an aqua regia solution for 4 h. The removal of Au was checked by X-ray photoelectron spectroscopy. For the functionalization of terpyridine ligand, the finally obtained cleaned porous Si (PS) substrate was initially dipped in a warm (60 °C) H$_2$O/NH$_4$OH/H$_2$O$_2$ (5:3:1, *v/v*) solution to make an OH-terminated surface. After that, for the surface functionalization with amino-silane, the OH-terminated PS substrate was dipped for 12 h in a 1% APTMS/methanol solution, then fully washed with pure methanol, and dried under nitrogen gas stream. The amino-silane functionalized substrate was then dipped in a 1 mM Tpy-COOH/DMSO solution for 6 h to finally functionalize terpyridine ligand on the surface. The terpyridine-functionalized substrate was abbreviated as PS-Si-Tpy.

For the electrochemical experiments of cyclic voltammetry and amperometry, a conventional three-electrode system was employed using a Potentiostat/Galvanostat (WPG100 model, WonATech Co., Ltd., Seoul, Korea). A Pt wire (0.5 mm) and Ag/AgCl electrodes were used as the counter and reference electrodes, respectively. Working electrodes were bare Si, bare PS, and terpyridine-functionalized PS (PS-Si-Tpy) substrates. A 0.1 M NaClO$_4$ solution was used as a supporting electrolyte with 10 mM Eu(III) ions. For electrodeposition of Eu on the three different substrates, the amperometry was performed at an applied potential of −1.8 V (vs. Ag/AgCl) for 5 h in a 10 mM Eu(III)/ 0.1 M NaClO$_4$ solution. The Eu-electrodeposited samples were further examined before and after thermal annealing at 700 °C.

For the surface morphologies of PS, Eu-electrodeposited PS and Eu-electrodeposited PS-Si-Tpy, a field-emission scanning electron microscope (model Hitachi S-4800 FE-SEM, Hitachi Ltd., Tokyo, Japan) was employed to take surface images. For the analysis of crystal phase formation, X-ray diffraction (XRD) patterns were obtained using a X-ray diffractometer (model MiniFlex II, Rigaku Corp., Tokyo, Japan, CNU chemistry core-facility) equipped with a Cu K_α X-ray light source. For crystal models, the VESTA software program (ver. 3.5.7) was used. To examine the major functional groups and the complex formation of the electrodeposited Eu materials before and after thermal annealing, FT-IR spectra were taken using a Nicolet iS 10 FT-IR spectrometer (Thermo Scientific Korea, Seoul, Korea) with an attenuated total reflection (ATR) mode. To examine photoluminescence (PL) characteristics of the Eu-electrodeposited Si, PS, and PS-Si-Tpy samples, a Sinco FS-2 fluorescence spectrometer (Sinco, Seoul, Korea) was used to obtain emission and excitation spectra, and their corresponding 2D and 3D photoluminescence (PL) counter maps scanned at various excitation wavelengths. The PL decay curves were taken using a FluoroLog 3 spectrometer (Horiba-Jobin Yvon, Kyoto, Japan) with a pulsed laser diode 374 nm ($\pm$10), a pulsed nano LED 264 nm ($\pm$10), and a single-photon-counting photomultiplier tube. X-ray photoelectron spectroscopy (XPS) was employed to confirm the surface oxidation states using a Thermo-VG Scientific K-alpha$^+$ spectrometer (Thermo VG Scientific, Waltham, MA, USA) equipped with a hemispherical energy analyzer and an Al K_α X-ray source.

3. Results

3.1. Suface Functionalization

The surface-functionalization process on a porous Si (PS) surface is depicted in Figure 1. As described in the experimental section, a PS substrate was initially terminated by OH groups. The surface was then functionalized with amino-silane. The amino group reacted with -COOH, forming a peptide bond [22,23]. Consequently, a terpyridine ligand was functionalized on the surface. The Lewis basic ligand strongly interacted with Lewis acidic metal cations such as the Eu(III) ion in the present study [22,23].
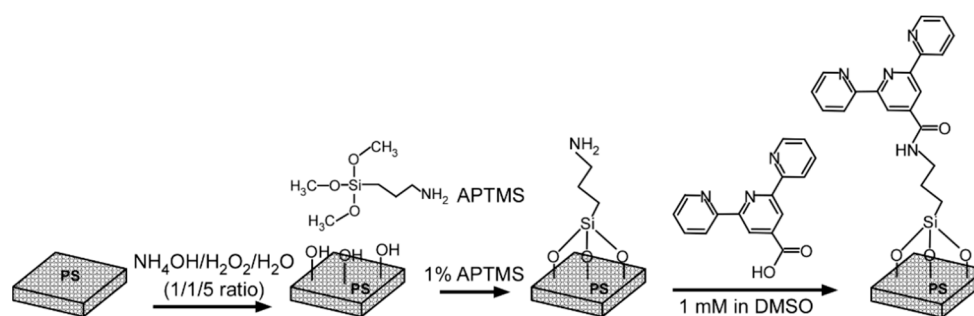

Figure 1. Surface functionalization process on a porous Si surface.

3.2. Suface Morphology of Porous Si and Electrodeposited Samples

Figure 2A,B display cyclic voltammetry (CV) profiles in 0.1 M NaClO$_4$ and 10 mM Eu(III)/0.1 M NaClO$_4$ electrolytes over PS and PS-Si-Tpy electrodes, respectively. A current increase (starting from -1.0 V in the negative-going potential) was commonly observed, attributed to a hydrogen-production reaction [22,23]. Upon addition of 10 mM Eu(III) ion, the current densities were enhanced by 1.5$\times$ and 1.7$\times$ at -1.8 V (vs. Ag/AgCl) over the PS and PS-Si-Tpy electrodes, respectively, due to the reduction/complexation current. For the functionalized electrode, the current density of hydrogen production current was relatively diminished. Therefore, the morphology after electrodeposition was expected to be different from that over PS, as discussed below. Figure 2a–d show the SEM images of Si after the first and second etching steps. As seen in Figure 2a, the Si surface was not fully etched by dipping in an HF solution. Furthermore, Au particles were still present on the surface. After the second etching step by electrochemistry, followed by Au removal, the SEM images showed submicron size pores well distributed on the surface shown in

Figure 2b. In the SEM image (Figure 2c) of the PS surface upon electrodeposition of Eu, clustered small particles were observed, and thin-film morphology was observed inside the pores. Upon thermal annealing at 700 °C, the surface was markedly changed, and small dots appeared to be embedded inside the pores. In the SEM image (Figure 2d) of the PS-Si-Tpy surface upon electrodeposition of Eu, thick films were appeared to be formed on the surface. The pores were fully covered by the electrodeposited materials. Upon thermal annealing of the sample, aggregated particles were found to be formed on the surface.
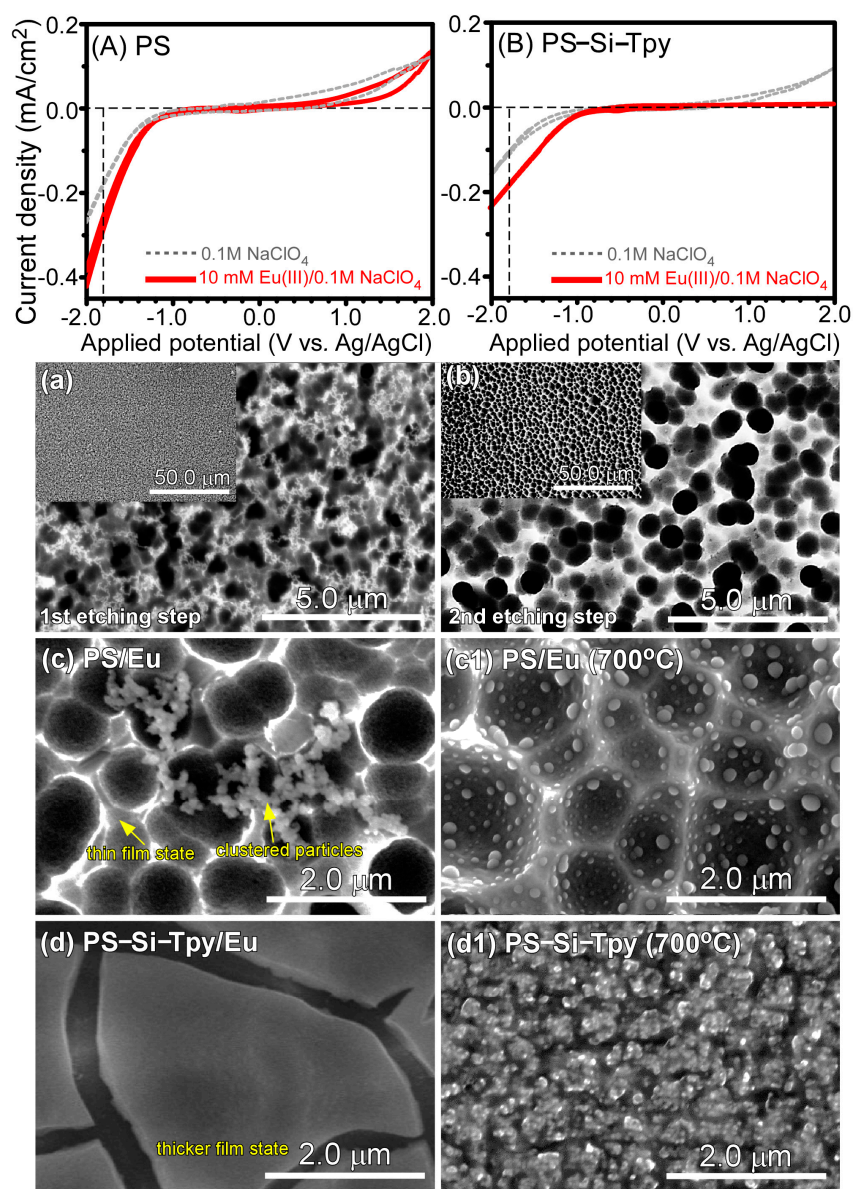

Figure 2. Cyclic voltammetry profiles of bare PS (**A**) and PS-Si-Tpy (**B**) in blank 0.1 M NaClO$_4$ (gray dotted line) and 0.1 M Eu(III)/0.1 M NaClO$_4$ (thick red line) electrolytes; SEM images of Si (**a**) after the first etching step, porous Si (**b**) after the second etching step, Eu-electrodeposited PS before (**c**) and after (**c1**) thermal annealing; and Eu-electrodeposited PS-Si-Tpy before (**d**) and after (**d1**) thermal annealing.

3.3. Crystal Phases of the As-Electrodeposited and Thermal-Annealed Samples

Figure 3 displays the XRD patterns of PS-Si-Tpy, Eu-electrodeposited PS-Si-Tpy, and thermal (700 °C) annealed Eu-electrodeposited PS-Si-Tpy samples. Before electrodeposition, the XRD signals were mainly due to bare Si [11]. Upon Eu deposition, new XRD peaks were clearly observed at 2θ = 10.1°, 20.1°, 28.0°, and 49.8°. Interestingly, these XRD

peak positions were in good consistency with those of the $Ln_2(OH)_x(NO_3)_y(SO_4)_z \cdot nH_2O$ complex [24], further discussed below. Joo et al. also reported similar XRD profiles for a series of lanthanide complexes on carbon and Ni substrates prepared by amperometry electrodeposition [25,26]. For the thermal-treated sample, several XRD peaks were observed at $2\theta = 28.5°$, $32.9°$, $47.3°$, and $56.1°$, a good match with the (222), (004), (044), and (226) crystal planes of cubic phase (Ia-3) Eu_2O_3 (ref. no 98-004-0472) [21]. The XRD peak at $2\theta = 28.5°$ was stronger than other peaks and corresponded to the (222) crystal plane. The unit cell structure and the structure projections of the (222) and (440) crystal planes are shown in the inset of Figure 3.
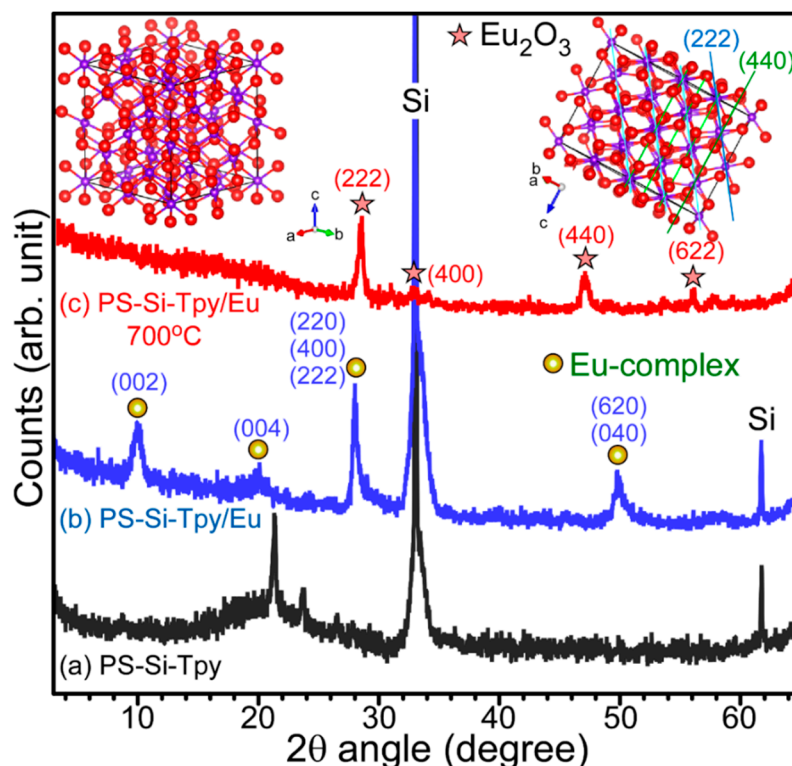

Figure 3. XRD profiles of porous Si (**a**), Eu-electrodeposited PS-Si-Tpy (**b**), and thermal-annealed PS-Si-Tpy/Eu (**c**), and the unit cell of Eu_2O_3 and the structure projections of the (222) and (440) crystal planes.

3.4. FT-IR of the As-Electrodeposited and Thermal-Annealed Samples

To confirm the major functional groups of a complex deduced from the XRD patterns, FT-IR spectra were taken and shown in Figure 4. Compared with the FT-IR profiles of PS (Figure 4a) and PS-Si-Tpy (Figure 4b) substrates, the substrates after Eu-electrodeposition showed strong transmittance FT-IR signals, and the two FT-IR profiles (Figure 4(a1,b1)) were observed to be very similar. This indicated that the complex formation was the same, although the corresponding morphologies (Figure 2) were different. A very strong and broad peak was observed around 3570 cm^{-1}, attributed to O–H stretching vibrations [21,25,26]. The O–H bending vibration appeared around 1620 cm^{-1}. A strong vibrational peak around 1100 cm^{-1} indicated a presence of ClO_4^- species trapped (or complexed) in the complex [25–27]. The peaks around 1350 cm^{-1} were attributed to the stretching modes of the CO_3^{2-} group [25,26]. The vibrational modes of the NO_3^- group also were found around this position [24]. Additional vibrational modes of CO_3^{2-} group were observed at 815 cm^{-1} and 935 cm^{-1}, confirming the presence of CO_3^{2-} group in the complex. The peak around 620 cm^{-1} could be assigned to a Eu–O vibrational mode [21,25,26]. On the basis of the FT-IR profiles, the complex of the electrodeposited materials possibly consisted of Eu, OH, H_2O, NO_3^-, and CO_3^{2-} groups. Upon thermal annealing at 700 °C, most of the peaks disappeared. The O-H vibrational

peaks were weakly observed, as expected. Two major peaks were observed at 1395 cm^{-1} and 1500 cm^{-1}, and were assigned to chemisorbed CO_2 species [21].
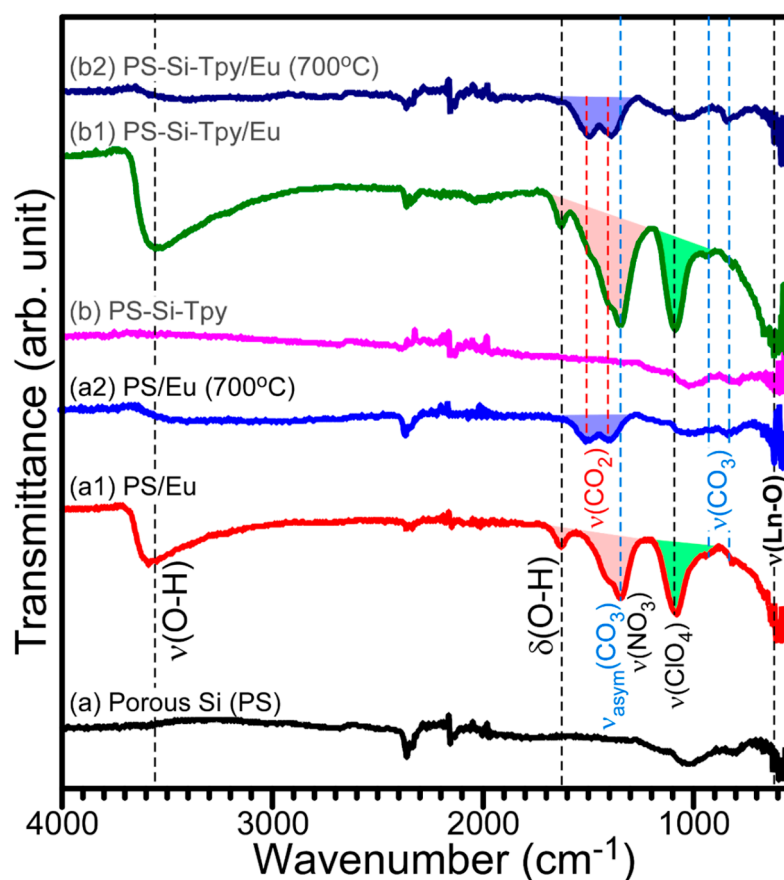

Figure 4. Transmittance FT-IR spectra of porous Si (**a**), Eu-deposited PS (**a1**), thermal-annealed PS/Eu (**a2**), terpyridine-functionalized PS (**b**), PS-Si-Tpy/Eu (**b1**), and thermal-annealed PS-Si-Tpy/Eu (**b2**).

3.5. Eu-Complexation with the Monolayer Terpyridine Ligand

Complexation of the Eu(III) ion with the functionalized terpyridine ligand was examined. This complexation occurred on the monolayer level, not on a bulk state by electrodeposition. A PS-Si-Tpy substrate was dipped in a 10 mM Eu(III)/0.1 M NaClO$_4$ solution for 1 h, gently rinsed with deionized water, and dried under a nitrogen gas stream. Photoluminescence spectroscopy and X-ray photoelectron spectroscopy were employed to confirm the complexation between the Eu(III) ion and the terpyridine group. For PS-Si-Tpy-Eu(III), Figure 5a displays the emission spectra taken at excitation wavelengths of 395 nm and 300 nm. The 395 nm corresponds to the $^5L_6 \leftarrow {}^7F_0$ direct excitation for Eu(III) energy levels [21]. Under this excitation, a broad peak was observed around 612 nm, attributed to the $^5D_0 \rightarrow {}^7F_2$ transition of the Eu(III) ion [21]. Under 300 nm excitation, two peaks were observed around 590 nm and 612 nm, assigned to the $^5D_0 \rightarrow {}^7F_1$ and $^5D_0 \rightarrow {}^7F_2$ transitions of the Eu(III) ion, respectively. The corresponding 2D and 3D photoluminescence contour maps (Figure 5(a1,a2)) show a more closely spaced region (or stronger signals) under 300 nm. This indicated that the Eu(III) emission was mainly excited by an indirect charge-transfer process from porous Si support to the Eu(III) site via the functionalized group.
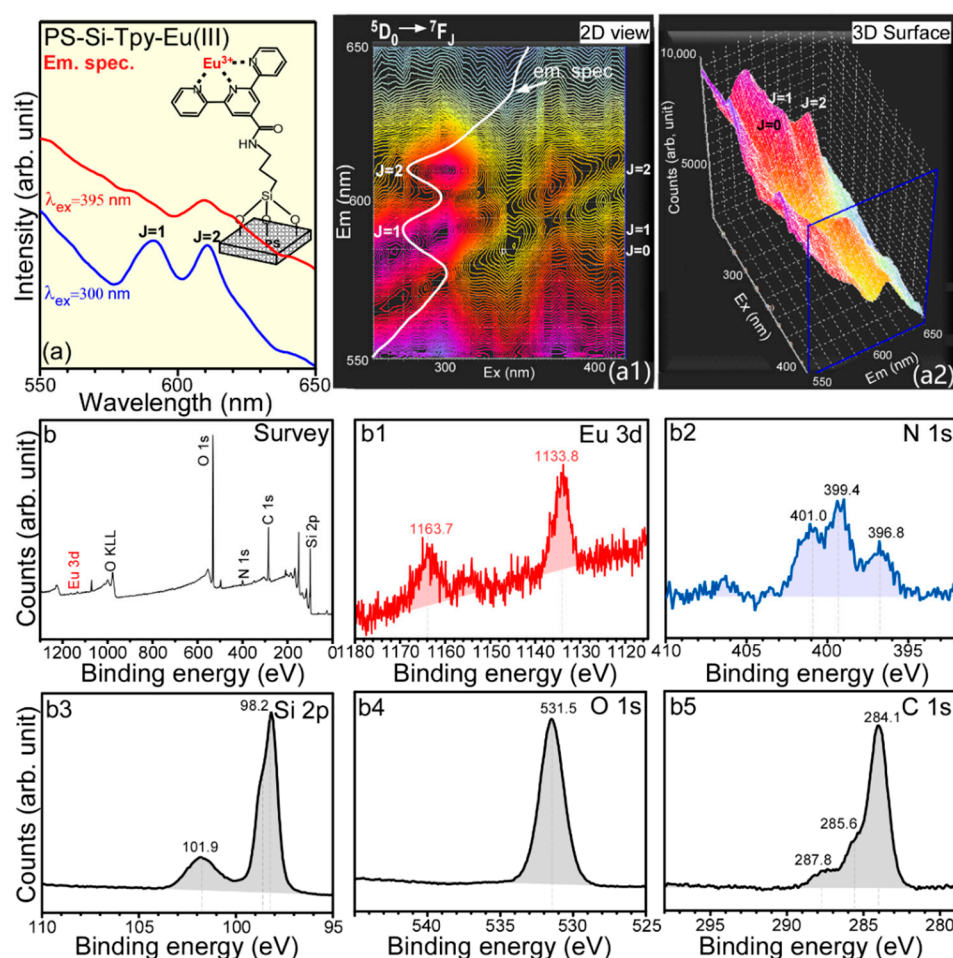
Figure 5. Emission spectra (**a**), corresponding 2D (**a1**), and 3D (**a2**) photoluminescence imaging profiles of Eu(III) coordinated with the functionalized terpyridine; and survey (**b**), Eu 3d (**b1**), N 1s (**b2**), Si 2p (**b3**), O 1s (**b4**), and C 1s (**b5**) XPS profiles.

Figure 5(b–b5) display the survey, Eu 3d, N 1s, Si 2p, O 1s, and C 1s XPS profiles for PS-Si-Tpy-Eu(III). Strong signals of Si, C, and O elements were expected from the PS and the functionalized molecules. The weak Eu 3d signal was due to Eu(III) complexed with the terpyridine ligand. Eu $3d_{5/2}$ and Eu $3d_{3/2}$ peaks were observed at 1133.8 eV and 1163.7 eV, and were attributed to the Eu(III) oxidation state [21,26]. Si 2p peaks were observed around 98.2 and 101.9 eV, and were attributed to Si^0 and Si-O species, respectively [11]. A strong O 1s peak at 531.5 eV was mainly due to Si-O species. Three N 1s peaks were observed, and were tentatively assigned to N of the amide bond (at 396.8 eV), and N of the singly (401.0 eV) and doubly (399.4 eV) coordinated terpyridine groups, respectively. The C 1s peaks at 284.1 eV, 285.6 eV, and 287.8 eV were attributed to C-C, C-N, and C-O species, respectively.

3.6. Photoluminescence of Electrodeposited Eu on the Si Substrate

Figure 6(a,a1) display the excitation and emission spectra for the Eu-electrodeposited Si substrate with no pores. The corresponding 2D and 3D photoluminescence contour maps are shown in Figure 6(c,c1), respectively. For the excitation spectra at emission wavelengths of 610 nm and 590 nm, weak peaks were observed around 280 nm and 395 nm, respectively. For the emission spectrum at an excitation wavelength of 280 nm, a broad peak was observed between 350 nm and 650 nm. The PL signals of Eu(III) ions were significantly observed between 550 nm and 720 nm. For the emission spectrum at 395 nm, weak signals appeared around 589 nm, 614 nm, 650 nm, and 690 nm, and were

attributed to the transitions from the excited $^5D_0$ level to the lower $^7F_1$, $^7F_2$, $^7F_3$, and $^7F_4$ levels, respectively [21,23].

Upon thermal annealing at 700 °C, the PL signals (Figure 6(b,b1)) were increased, due to a change in the crystal phase and a decrease in the PL quenching centers. In the excitation spectrum at an emission wavelength of 610 nm, the several peaks at 365 nm, 382 nm, 395 nm, and 405 nm were assigned to the transitions from the ground $^7F_0$ level to the upper $^5D_4$, $^5G_J/^5L_7$, $^5L_6$, and $^5D_3$ levels, respectively [21,23]. A much stronger (2×) and broader peak was observed around 280 nm, commonly attributed to a charge-transfer ($O^{2-} \rightarrow Eu^{3+}$) excitation [21,23]. For the excitation spectrum at 590 nm, a broad peak around 280 nm was mainly observed. For the emission spectrum at an excitation wavelength of 280 nm, two sharp peaks appeared at 588 nm and 611 nm, and were attributed to the transitions from the excited $^5D_0$ level to the lower $^7F_1$ and $^7F_2$ levels, respectively [21,23]. On the other hand, for the emission spectrum at 395 nm, the peak at 611 nm was mainly observed, and the peak at 588 nm was drastically diminished. The corresponding 2D and 3D photoluminescence contour maps taken at various excitation wavelengths are shown in Figure 6(d,d1), respectively.
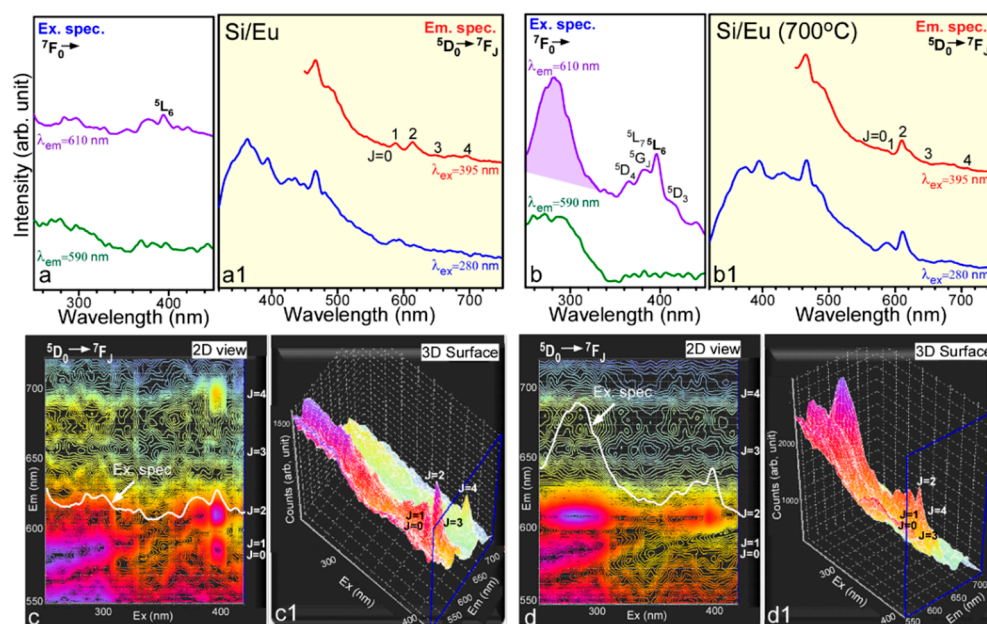

Figure 6. Excitation (**a**,**b**) and emission (**a1**,**b1**) spectra for electrodeposited Eu on Si (**left panel**) and thermal-annealed Si/Eu (**right panel**), and their 2D (**c**,**c1**) and 3D (**d**,**d1**) photoluminescence imaging profiles.

3.7. Photoluminescence of Electrodeposited Eu on the Porous Si Substrate

Figure 7(a,a1) display the excitation and emission spectra for a porous Si substrate after Eu electrodeposition, respectively. Compared with the PL signals in Figure 6, the PL intensity was strongly enhanced by about 11×. In the excitation spectrum at an emission wavelength of 612 nm, several peaks were observed around 295 nm, 320 nm, 364 nm, 381 nm, 395 nm, and 415 nm, and were attributed to the transitions from the $^7F_0$ level to the upper $^5F_4$, $^5H_5$, $^5D_4$, $^5G_J/^5L_7$, $^5L_6$, and $^5D_3$, levels, respectively [21,23]. The peak at 395 nm was major. In the excitation spectrum at 590 nm, the sharper peaks were somewhat weakened, while the peak around 290 nm was increased. For the emission spectra at an excitation wavelength of 290 nm, no characteristics of Eu(III) PL signals were significantly observed. However, the emission spectrum at 395 nm showed sharp PL signals around 575 nm, 591 nm, 612 nm, 650 nm, and 697 nm, attributed to the transitions from the excited $^5D_0$ level to the lower $^7F_1$, $^7F_2$, $^7F_3$, and $^7F_4$ levels, respectively, as mentioned above [21,23]. The corresponding 2D and 3D photoluminescence contour maps are shown in Figure 7(c,c1), respectively.

Upon thermal annealing at 700 °C, the PL profiles (Figure 7(b,b1)) were drastically changed, and the intensity was also substantially increased by about 29×. One major change was found in the excitation spectra at excitation wavelengths of 614 nm and 590 nm. In the excitation spectrum at 614 nm, the charge-transfer peak at 295 nm was observed to be about 5.1× stronger than the peak at 395 nm. In the excitation spectrum at 590 nm, the charge-transfer peak was mainly observed, and no transition signals of Eu(III) ions were significantly observed between 350 nm and 450 nm. In the emission spectrum at 295 nm, two major peaks were observed at 594 nm ($^5D_0 \rightarrow {}^7F_1$) and 613 nm ($^5D_0 \rightarrow {}^7F_2$). On the other hand, in the emission spectrum at 395 nm, a peak at 614 nm ($^5D_0 \rightarrow {}^7F_2$) was mainly observed. The peak at 697 nm ($^5D_0 \rightarrow {}^7F_4$) was observed to be substantially decreased upon thermal annealing. The corresponding 2D and 3D photoluminescence contour maps are shown in Figure 7(d,d1), respectively.
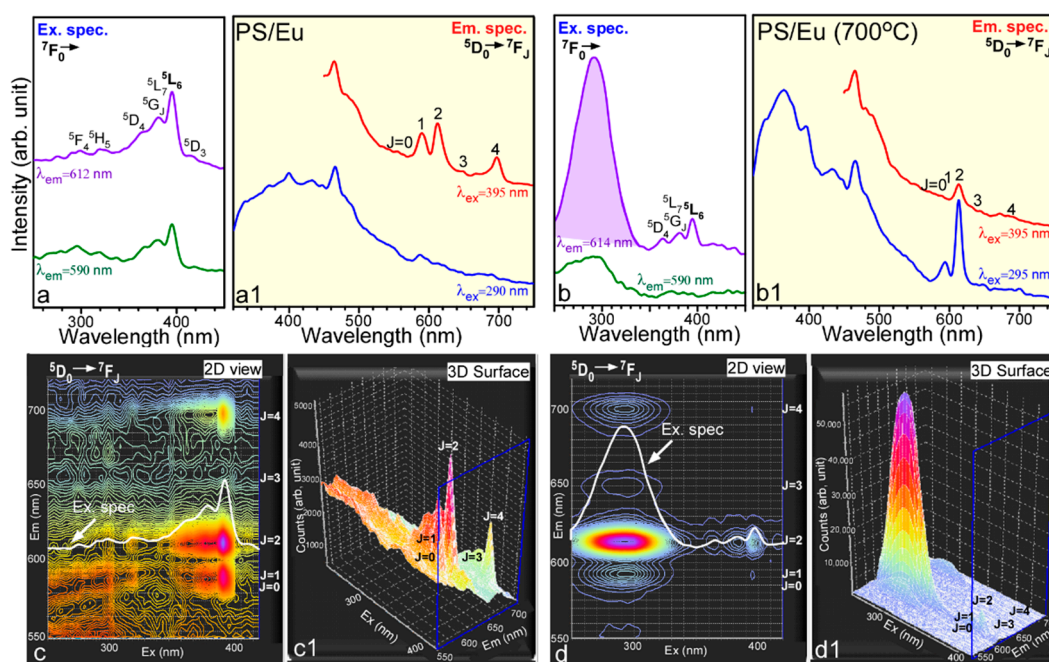

Figure 7. Excitation (**a**,**b**) and emission (**a1**,**b1**) spectra for electrodeposited Eu on PS (**left panel**) and thermal-annealed PS/Eu (**right panel**), and their 2D (**c**,**c1**) and 3D (**d**,**d1**) photoluminescence imaging profiles.

3.8. Photoluminescence of Electrodeposited Eu on the PS-Si-Tpy Substrate

Figure 8(a,a1) displays excitation and emission spectra for the PS-Si-Tpy substrate after Eu electrodeposition, respectively. The PL profiles were quite similar to those of the PS substrate after Eu electrodeposition shown in Figure 7. One difference is that the PL intensity was weaker (by about 0.2×) than those shown in Figure 7. The peak positions and the corresponding assignments were the same, as discussed above. The corresponding 2D and 3D photoluminescence contour maps are shown in Figure 8(c,c1), respectively. Upon thermal annealing at 700 °C, the PL profiles (Figure 8(b,b1)) were also drastically changed, and the intensity was also substantially increased, as shown in Figure 7. The peak positions and profiles were also very similar to those found in Figure 7(b,b1). In the excitation spectrum at 614 nm, the charge-transfer peak at 295 nm was observed to be about 7.8× stronger than the peak at 395 nm. The corresponding 2D and 3D photoluminescence contour maps are shown in Figure 8(d,d1), respectively.
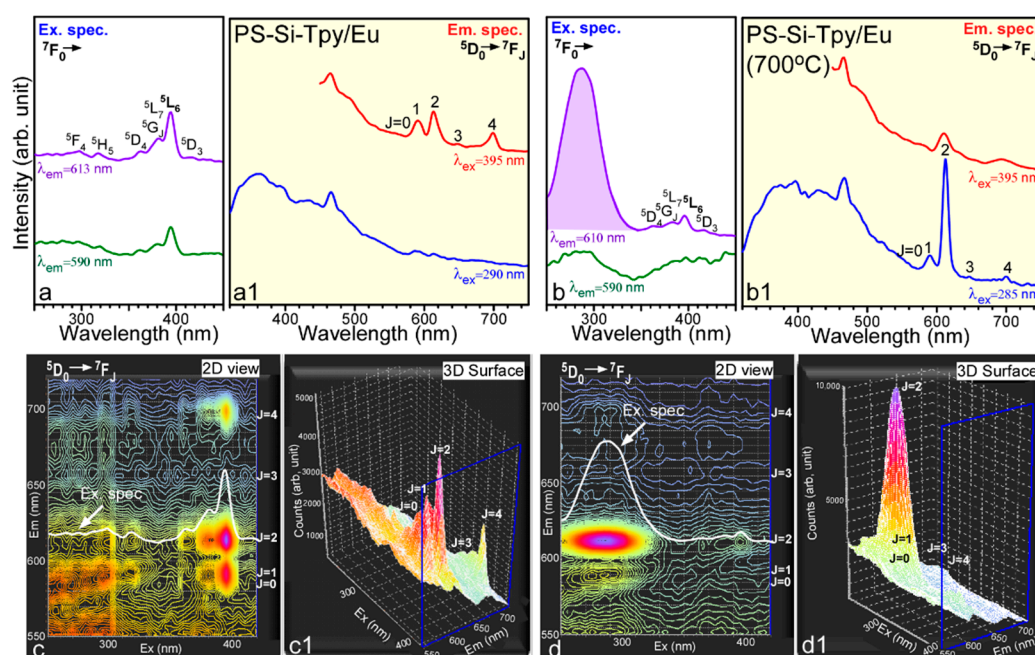
Figure 8. Excitation (**a**,**b**) and emission (**a1**,**b1**) spectra for electrodeposited Eu on terpyridine-functionalized PS (**left panel**) and thermal-annealed PS-Si-Tpy/Eu (**right panel**), and their 2D (**c**,**c1**) and 3D (**d**,**d1**) photoluminescence imaging profiles.

3.9. Photoluminescence Decay Kinetics

Figure 9 displays photoluminescence decay profiles at an emission wavelength of 610 nm, corresponding to the $^5D_0 \rightarrow {}^7F_2$ transition. The fitting parameters are summarized in Table 1 using a third-order exponential decay function [23]. The average lifetimes at an excitation wavelength of 374 nm were estimated to be 18.7 ns and 23.4 ns for the PS-Si-Tpy/Eu and thermal-annealed PS-Si-Tpy/Eu samples, respectively. The as-electrodeposited sample showed a shorter lifetime. The lifetime at an excitation wavelength of 264 nm was much shorter, at 15.4 ns.
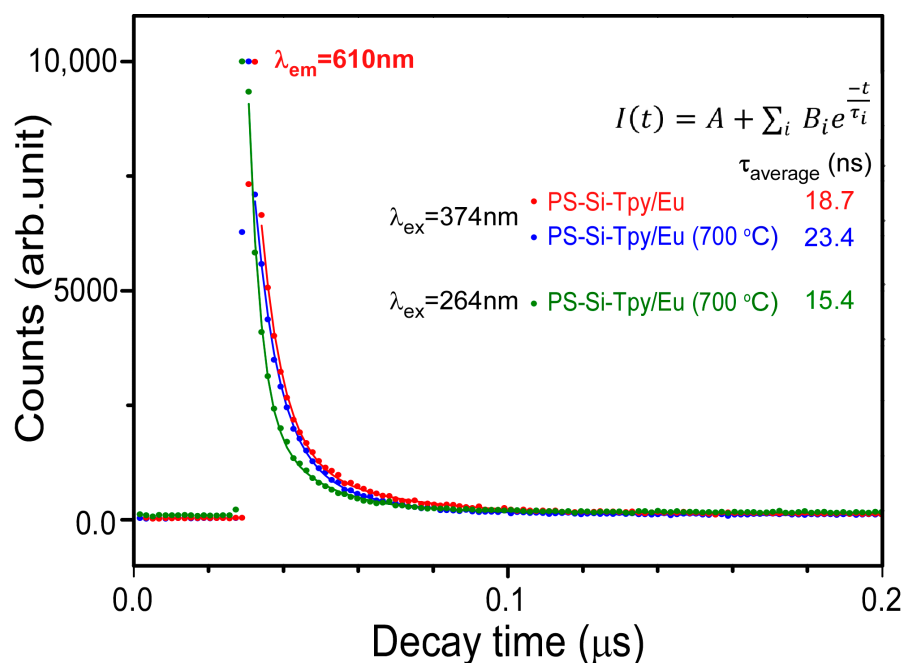

Figure 9. Photoluminescence decay times for 610 nm emission signals at excitation wavelengths of 264 nm and 374 nm for the PS-Si-Tpy/Eu and thermal-annealed PS-Si-Tpy/Eu samples.

Table 1. Fitting parameters of the PL decay curves for 610 nm emission signals at excitation wavelengths of 264 nm and 374 nm for the PS-Si-Tpy/Eu and thermal-annealed PS-Si-Tpy/Eu samples.

Parameters	PS-Si-Tpy/Eu (374 nm)	PS-Si-Tpy/Eu-700 °C (374 nm)	PS-Si-Tpy/Eu-700 °C (264 nm)
τ_1 (ns)	19.58	25.34	14.75
τ_2 (ns)	798.36	867.749	1102.64
τ_3 (ns)	6.18	5.94	3.19
B_1	1558.68	1360.836	2288.291
B_2	83.2513	98.52946	76.09427
B_3	5271.567	4926.381	6620.526
R_1	0.2254	0.2131	0.2547
R_2	0.0120	0.0154	0.0085
R_3	0.7625	0.7715	0.7368
A	34.77629	37.63854	93.39494
χ^2	1.066872	1.102067	1.091194
$\tau_{average}$ (ns)	18.74 ($\pm$0.20)	23.37 ($\pm$0.24)	15.44 ($\pm$0.24)

Note: $I(t) = A + \sum_i B_i e^{\frac{-t}{\tau_i}}$, $R_i = B_i/(\sum_{i=1}^{3} B_i)$, $\tau_{average} = \sum_{i=1}^{3} R_i \cdot \tau_i$, R = the relative ratio factor.

3.10. Surface Chemical States of the Electrodeposited Materials

Figure 10 displays the survey, Eu 3d, and O 1s XPS profiles of the PS-Eu and PS-Si-Tpy-Eu before and after thermal annealing. The survey spectra commonly showed the elements of Eu (Eu 3d, Eu 4s, Eu 4p, and Eu 4d), O (O 1s), and C (C 1s), as expected. For the as-electrodeposited samples before thermal annealing, additional peaks were observed at binding energies (BEs) of 407 eV and 208 eV, and were attributed to N of NO_3^- and Cl of ClO_4^-, respectively [23,25,26]. These two groups were observed in the FT-IR spectra (Figure 4). Upon thermal annealing, these two elements disappeared. For the Eu 3d XPS profiles before thermal annealing, the Eu $3d_{5/2}$ and Eu $3d_{3/2}$ peaks were observed at 1133.8 eV and 1163.5 eV, respectively, with a spin-orbit splitting energy of 29.7 eV, which was attributed to the Eu(III) oxidation state [21,28]. No indication of the Eu(II) oxidation state was found. Upon thermal annealing, the Eu $3d_{5/2}$ and Eu $3d_{3/2}$ peaks were observed at 1135.0 eV and 1164.8 eV, respectively, with a spin-orbit splitting energy of 29.8 eV, which was attributed to the Eu(III) oxidation state. Interestingly, two additional peaks were found around 1126 eV and 1156 eV; these were attributed to the Eu $3d_{5/2}$ and Eu $3d_{3/2}$ peaks of the Eu(II) oxidation state. For the O 1s XPS profiles before thermal annealing, two peaks could be assigned at 530.5 eV and 532.0 eV; these were attributed to the Eu-OH and C-O/ClO_4 species, respectively [23,25,26]. Upon thermal annealing, three peaks could be assigned at 528.2 eV, 530.2 eV and 532.2 eV; these were attributed to lattice oxygen, defect oxygen, and surface O-H/H_2O species, respectively [23,25,26]. The dominant O 1s peak at 532.2 eV could be due to the hygroscopic nature of Eu_2O_3 [21]. The defect-related peak was plausibly due to the existence of two oxidation states of Eu(III) and Eu(II) ions after thermal annealing.
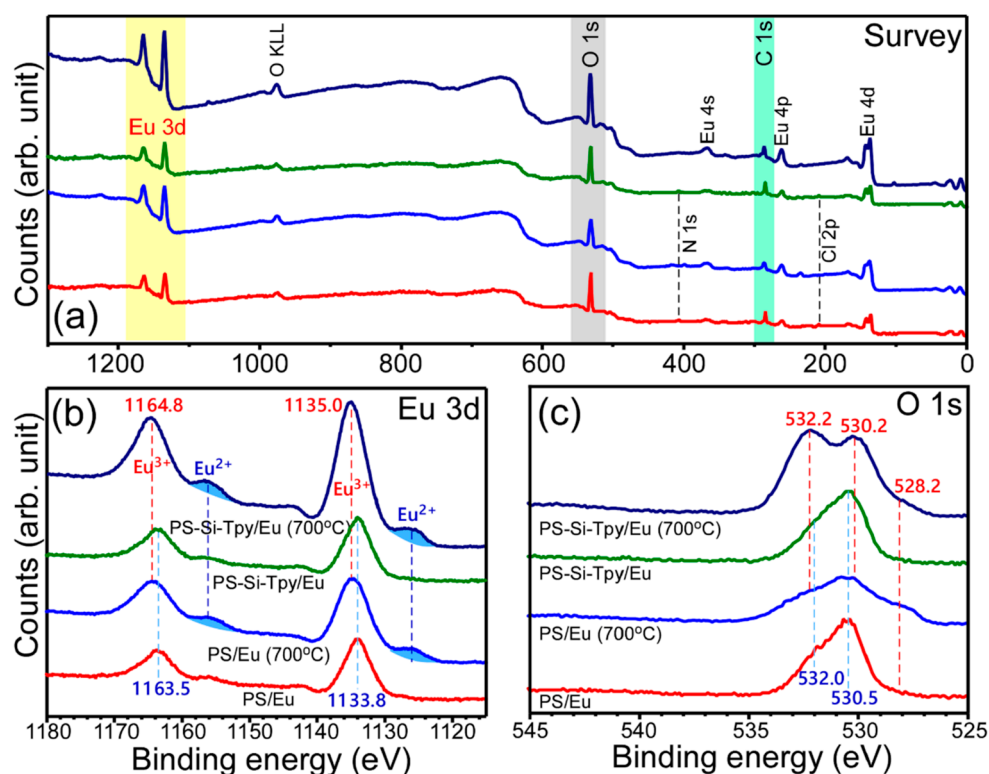
Figure 10. Survey (**a**), Eu 3d (**b**), and O 1s (**c**) XPS profiles of PS-Eu and PS-Si-Tpy-Eu before and after thermal annealing.

4. Discussion

Eu electrodeposition on both PS and terpyridine-functionalized PS (PS-Si-Tpy) were observed to be successful. It was initially assumed that light absorption and emission are both increased when Eu species were deposited on a PS with a high surface area. Moreover, when it was applied to an electrode catalyst material, the catalytic surface area was increased, and finally, the catalytic performance was enhanced. On the basis of the CV profiles, the currents at the applied potential were due to hydrogen evolution reaction and Eu complexation process. Thereby, the morphologies over the two different surfaces were expected to be different. SEM images (Figure 2) confirmed Eu was deposited inside the pores of PS. On the PS-Si-Tpy substrate, the film that was formed was thicker, and the pores were fully covered by the film. The uniform film formation on the PS-Si-Tpy electrode could be because the terpyridine ligand initially interacted with the Eu(III) ion that may initiate uniform electrodeposition. The interaction between Eu(III) ion and the terpyridine group was evidenced by PL and XPS (Figure 5). The Eu(III) emission characteristics were observed in the PL profiles at both direct and indirect excitation wavelengths. The PL intensity was stronger at an indirect (charge-transfer) excitation wavelength of 300 nm, compared with that at a direct excitation. This indicated that the Eu(III) ion was well bound with the terpyridine group. Thereby, a charge-transfer effect was observed to be efficient. The higher N 1s BE position also indicated an interaction between Eu(III) ions and three N atoms of the terpyridine group.

The materials were observed to be electrodeposited as a form of $Eu_2(OH)_x(NO_3)_y$ $(CO_3)_z \cdot nH_2O$ complex [24–26]. One of several experimental evidences was the vibrational modes of H_2O/OH, CO_3^{2-}, and NO_3^- species in the FT-IR spectra (Figure 4). Another evidence was the XRD profile (Figure 3) of the corresponding sample. Wu et al. reported a very similar XRD profile for a $Ln_2(OH)_5(SO_4)_x(NO_3)_y \cdot nH_2O$ complex. On the basis of the literature, when SO_4^{2-} is replayed by CO_3^{2-}, we expect a similar complex formation, as well as a similar XRD profile. At a fixed potential during electrodeposition, an electric double layer (positive and negative ions) is commonly formed. Therefore, in the

present electrochemical condition the positive Lewis acidic Eu(III) ions and the negative Lewis basic species (H_2O/OH, CO_3^{2-} and NO_3^- species) are expected to form a double layer and complexed by the interaction. The carbonate ion formation and complexation with metal cations have commonly been reported via $CO_2 + H_2O \rightarrow 2H^+ + CO_3^{2-}$ and $M^{n+} + CO_3^{2-} \rightarrow MCO_3$ [29]. The hydrogen ion is plausibly reduced via $2H^+ + 2e^- \rightarrow H_2$ in the negative potential. The oxidation state of Eu was observed to be purely +3 for the complex, evidenced by the XPS data (Figure 10). When the electrodeposited materials were thermal-annealed at 700 °C, the XRD profile was totally changed, and a cubic Eu_2O_3 crystal phase was observed. The Eu_2O_3 was more tightly embedded inside the pores of the PS.

For the PL profiles of the as-electrodeposited samples, PL signals for the Eu(III) ion were detected mainly under direct excitation into upper Eu(III) energy levels from the $^7F_0$ level to the upper $^5F_4$, $^5H_5$, $^5D_4$, $^5G_J/^5L_7$, $^5L_6$, and $^5D_3$ levels. The PL intensities of the as-electrodeposited samples were significantly lower than those of the corresponding thermal-treated samples. The lower intensity was due to lower crystallinity and PL quenching centers such as H_2O/OH [30]. The presence of H_2O/OH was clearly evidenced by the FT-IR spectra. The two major emission signals around 590 nm and 610 nm were attributed to the $^5D_0 \rightarrow {}^7F_1$ and $^5D_0 \rightarrow {}^7F_2$ transitions, respectively. The $^5D_0 \rightarrow {}^7F_1$ is a magnetic dipole transition, and insensitive to the environment of the Eu(III) ion [21]. On the other hand, the $^5D_0 \rightarrow {}^7F_2$ is an electric dipole transition, and sensitive to the local environment. For the PL profiles at an excitation wavelength of 395 nm, the $(^5D_0 \rightarrow {}^7F_2)/(^5D_0 \rightarrow {}^7F_1)$ intensity ratios were estimated to be 1.89, 1.49, and 1.63 for the Si, PS, and PS-Si-Tpy electrodes, respectively. This reflects that the Eu(III) complex on PS had a more symmetric character. For the thermal-annealed samples, the $^5D_0 \rightarrow {}^7F_2$ transition emission signal under 395 nm was dominantly seen, and the $^5D_0 \rightarrow {}^7F_1$ transition emission signal was extremely weaker than the $^5D_0 \rightarrow {}^7F_2$ transition. This reflects that the electric dipole transition dominated, and the Eu(III) ion was positioned at the less-symmetric site. For the PL profiles at an indirect excitation, the $(^5D_0 \rightarrow {}^7F_2)/(^5D_0 \rightarrow {}^7F_1)$ intensity ratios were estimated to be 2.36, 3.95, and 7.0 for the Si, PS, and PS-Si-Tpy electrodes, respectively. The measured lifetime (24 ns) of Eu_2O_3 on PS at the $^5D_0 \rightarrow {}^7F_2$ transition was observed to be much shorter than other systems, such as Eu_2O_3 powder with a lifetime of 25 μs [21]. The red ($^5D_0 \rightarrow {}^7F_2$ transition) emission in the Eu_2O_3 powder was mainly due to a direct excitation to an Eu(III) energy level. On the other hand, the red emission for Eu_2O_3 on PS originated from strong coupling between the PS and Eu via an oxygen bridge. Therefore, the shortening of the PL lifetime was presumably due to the coupling. Park et al. reported longer lifetimes of 0.17–0.68 μs (170–680 ns) for Eu complexes on ITO surfaces electrodeposited in a 10 mM Eu(III)/0.1 M $NaClO_4$ electrolyte condition [22]. In the present study, the average lifetime was estimated to be 0.0187 μs (18.7 ns) for the Eu complex on PS-Si-Tpy support. The shorter lifetime was also attributed to a PS support effect.

5. Conclusions

Electrodeposition of an Eu(III) complex was successfully demonstrated on porous Si and terpyridine-functionalized porous Si surfaces by amperometry. On the basis of FT-IR, XPS, and XRD data, the electrodeposited material was tentatively concluded to be an $Eu_2(OH)_x(NO_3)_y(CO_3)_z \cdot nH_2O$ complex. This complex was converted to cubic phase Eu_2O_3 upon thermal annealing at 700 °C. Eu_2O_3 was observed to be well embedded inside Si pores. For the complexation of terpyridine, the Eu(III) ion was well coordinated with a terpyridine ligand with three N atoms, based on the PL and XPS profiles. For as-electrodeposited materials, photoluminescence signals of Eu(III) were mainly due to a direct excitation of 395 nm, corresponding to the transition from the $^7F_0$ level to the upper $^5L_6$ level. For thermal-treated materials, the strongly enhanced PL signals were mainly due to charge-transfer ($O^{2-} \rightarrow Eu^{3+}$) excitation between 280 nm and 300 nm. This charge-transfer effect was dominant for the PS support. The PL signal intensity for electrodeposited Eu on PS showed the highest and was much stronger than others on Si and terpyridine-functionalized PS, respectively. The strongly enhanced luminescence was

attributed to the PS support effect. The present results demonstrate that the porous surface state significantly enhanced photoluminescence signals, and provide valuable information on the development of display materials and thin-film electrodes.

Data Availability Statement: The data presented in this study are available in article.

Conflicts of Interest: The authors declare no conflict of interest.

References

1. Chen, X.; Bi, Q.; Sajjad, M.; Wang, X.; Ren, Y.; Zhou, X.; Xu, W.; Liu, Z. One-Dimensional Porous Silicon Nanowires with Large Surface Area for Fast Charge–Discharge Lithium-Ion Batteries. *Nanomaterials* **2018**, *8*, 285. [CrossRef] [PubMed]
2. Li, W.; Liu, Z.; Fontana, F.; Ding, Y.; Liu, D.; Hirvonen, J.T.; Santos, H.A. Tailoring Porous Silicon for Biomedical Applications: From Drug Delivery to Cancer Immunotherapy. *Adv. Mater.* **2018**, *30*, 1703740. [CrossRef] [PubMed]
3. Arshavsky-Graham, S.; Massad-Ivanir, N.; Segal, E.; Weiss, S. Porous Silicon-Based Photonic Biosensors: Current Status and Emerging Applications. *Anal. Chem.* **2019**, *91*, 441–467. [CrossRef]
4. Rezvani, S.J.; Pinto, N.; Gunnella, R.; D'Elia, A.; Marcelli, A.; Di Cicco, A. Engineering Porous Silicon Nanowires with Tuneable Electronic Properties. *Condens. Matter* **2020**, *5*, 57. [CrossRef]
5. Coffer, J.L.; Canham, L.T. Nanoporous Silicon as a green, high-tech educational tool. *Nanomaterials* **2021**, *11*, 553. [CrossRef] [PubMed]
6. Miranda, C.R.B.; Baldan, M.R.; Beloto, A.F.; Ferreira, N.G. Morphological and Optical Characteristics of Porous Silicon Produced by Anodization Process in HF-Acetonitrile and HF-Ethanol Solutions. *J. Braz. Chem. Soc.* **2008**, *19*, 769–774. [CrossRef]
7. Balderas-Valadez, R.F.; Agarwal, V.; Pacholski, C. Fabrication of Porous Silicon-Based Optical Sensors Using Metal-Assisted Chemical Etching. *RSC Adv.* **2016**, *6*, 21430–21434. [CrossRef]
8. Entwistle, J.; Rennie, A.; Patwardhan, S.A. Review of Magnesiothermic Reduction of Silica to Porous Silicon for Lithium-Ion Battery Applications and Beyon. *J. Mater. Chem. A* **2018**, *6*, 18344–18356. [CrossRef]
9. De Stefano, L. Porous Silicon Optical Biosensors: Still a Promise or a Failure? *Sensors* **2019**, *19*, 4776. [CrossRef]
10. Terracciano, M.; Rea, I.; Borbone, N.; Moretta, R.; Oliviero, G.; Piccialli, G.; De Stefano, L. Porous Silicon-Based Aptasensors: The Next Generation of Label-Free Devices for Health Monitoring. *Molecules* **2019**, *24*, 2216. [CrossRef]
11. Jia, H.; Zheng, J.; Song, J.; Luo, L.; Yi, R.; Estevez, L.; Zhao, W.; Patel, R.; Li, X.; Zhang, J.-G. A Novel Approach to Synthesize Micrometer-Sized Porous Silicon as a High Performance Anode for Lithium-Ion Batteries. *Nano Energy* **2018**, *50*, 589–597. [CrossRef]
12. Moretta, R.; De Stefano, L.; Terracciano, M.; Rea, I. Porous Silicon Optical Devices: Recent Advances in Biosensing Applications. *Sensors* **2021**, *21*, 1336. [CrossRef]
13. Sundarapura, P.; Zhang, X.-M.; Yogai, R.; Murakami, K.; Fave, A.; Ihara, M. Nanostructure of Porous Si and Anodic SiO_2 Surface Passivation for Improved Efficiency Porous Si Solar Cells. *Nanomaterials* **2021**, *11*, 459. [CrossRef] [PubMed]
14. Ramírez-González, F.; García-Salgado, G.; Rosendo, E.; Díaz, T.; Nieto-Caballero, F.; Coyopol, A.; Romano, R.; Luna, A.; Monfil, K.; Gastellou, E. Porous Silicon Gas Sensors: The Role of the Layer Thickness and the Silicon Conductivity. *Sensors* **2020**, *20*, 4942. [CrossRef] [PubMed]
15. Dwivedi, P.; Chauhan, N.; Vivekanandan, P.; Das, S.; Kumar, D.S.; Dhanekar, S. Scalable Fabrication of Prototype Sensor for Selective and Sub-ppm Level Ethanol Sensing Based on TiO_2 Nanotubes Decorated Porous Silicon. *Sens. Actuators B* **2017**, *249*, 602–610. [CrossRef]
16. Kim, T.; Fu, X.; Warther, D.; Sailor, M.J. Size-controlled Pd nanoparticle catalysts prepared by galvanic displacement into a porous Si-Iron oxide nanoparticle host. *ACS Nano* **2017**, *11*, 2773–2784. [CrossRef] [PubMed]
17. Ortaboy, S.; Alper, J.P.; Rossi, F.; Bertoni, G.; Salviati, G.; Carraro, C.; Maboudian, R. MnO_x-Decorated Carbonized Porous Silicon Nanowire Electrodes for High Performance Supercapacitors. *Energy Environ. Sci.* **2017**, *10*, 1505–1516. [CrossRef]
18. Lee, S.H.; Kang, J.S.; Kim, D. A Mini Review: Recent Advances in Surface Modification of Porous Silicon. *Materials* **2018**, *11*, 2557. [CrossRef]
19. Salonen, J.; Mäkilä, E. Thermally Carbonized Porous Silicon and Its Recent Applications. *Adv. Mater.* **2018**, *30*, 1703819. [CrossRef]
20. Yaghoubi, M.; Rahimi, F.; Negahdari, B.; Rezayan, A.H.; Shafiekhani, A. A Lectin-Coupled Porous Silicon-Based Biosensor: Label-Free Optical Detection of Bacteria in a Real-Time Mode. *Sci. Rep.* **2020**, *10*, 16017. [CrossRef]

21. Kang, J.-G.; Jung, Y.; Min, B.-K.; Sohn, Y. Full characterization of Eu(OH)$_3$ and Eu$_2$O$_3$ nanorods. *Appl. Surf. Sci.* **2014**, *314*, 158–165. [CrossRef]

22. Park, S.J.; Joo, M.H.; Hong, S.-M.; Rhee, C.K.; Kang, J.-G.; Sohn, Y. Electrochemical Eu(III)/Eu(II) Behaviors and Recovery over Terpyridyl-Derivatized Modified Indium Tin Oxide Electrode Surfaces. *Chem. Eng. J.* **2021**, *15*, 128717. [CrossRef]

23. Park, S.J.; Joo, M.H.; Hong, S.-M.; Kang, J.-G.; Rhee, C.K.; Lee, S.W.; Sohn, Y. Electrochemical Eu(III) behaviors and Eu oxysulfate recovery over terpyridine-functionalized indium tin oxide electrode. *Inorg. Chem. Front.* **2020**, *8*, 1175–1188. [CrossRef]

24. Wu, X.; Li, J.-G.; Zhu, Q.; Liu, W.; Li, J.; Li, X.; Sun, X.; Sakka, Y. One-step freezing temperature crystallization of layered rare-earth hydroxide (Ln$_2$(OH)$_5$NO$_3$·nH$_2$O) nanosheets for a wide spectrum of Ln (Ln = Pr–Er, and Y), anion exchange with fluorine and sulfate, and microscopic coordination probed via photoluminescence. *J. Mater. Chem. C* **2015**, *3*, 3428–3437. [CrossRef]

25. Joo, M.H.; Park, S.J.; Hong, S.M.; Rhee, C.K.; Sohn, Y. Electrochemical recovery and behaviors of rare earth (La, Ce, Pr, Nd, Sm, Eu, Gd, Tb, Dy, Ho, Er, Tm, and Yb) ions on Ni sheets. *Materials* **2020**, *13*, 5314. [CrossRef]

26. Joo, M.H.; Park, S.J.; Hong, S.-M.; Rhee, C.K.; Kim, D.; Sohn, Y. Electrodeposition and Characterization of Lanthanide Elements on Carbon Sheets. *Coatings* **2021**, *11*, 100. [CrossRef]

27. Chen, Y.; Zhang, Y.-H.; Zhao, L.-Z. ATR-FTIR spectroscopic studies on aqueous LiClO$_4$, NaClO$_4$, and Mg(ClO$_4$)$_2$ solutions. *Phys. Chem. Chem. Phys.* **2004**, *6*, 537–542. [CrossRef]

28. NIST X-ray Photoelectron Spectroscopy Database, Version 4.1 National Institute of Standards and Technology, Gaithersburg. 2012. Available online: http://srdata.nist.gov/xps/ (accessed on 2 April 2021).

29. Millero, F.J.; Magdalena Santana-Casiano, J.; Gonzalez-Davila, M. The formation of Cu(II) complexes with carbonate and bicarbonate ions in NaClO$_4$ solutions. *J. Solut. Chem.* **2010**, *39*, 543–558. [CrossRef]

30. Sohn, Y. Structural and spectroscopic characteristics of terbium hydroxide/oxide nanorods and plates. *Ceram. Int.* **2014**, *40*, 13803–13811. [CrossRef]